



Prediction of microstructure, residual stress, and deformation in laser powder bed fusion process

Y. P. Yang¹ · M. Jamshidinia¹ · P. Boulware¹ · S. M. Kelly¹

Received: 15 September 2017 / Accepted: 8 December 2017 / Published online: 12 December 2017
© Springer-Verlag GmbH Germany, part of Springer Nature 2017

Abstract

Laser powder bed fusion (L-PBF) process has been investigated significantly to build production parts with a complex shape. Modeling tools, which can be used in a part level, are essential to allow engineers to fine tune the shape design and process parameters for additive manufacturing. This study focuses on developing modeling methods to predict microstructure, hardness, residual stress, and deformation in large L-PBF built parts. A transient sequentially coupled thermal and metallurgical analysis method was developed to predict microstructure and hardness on L-PBF built high-strength, low-alloy steel parts. A moving heat-source model was used in this analysis to accurately predict the temperature history. A kinetics based model which was developed to predict microstructure in the heat-affected zone of a welded joint was extended to predict the microstructure and hardness in an L-PBF build by inputting the predicted temperature history. The tempering effect resulting from the following built layers on the current-layer microstructural phases were modeled, which is the key to predict the final hardness correctly. It was also found that the top layers of a build part have higher hardness because of the lack of the tempering effect. A sequentially coupled thermal and mechanical analysis method was developed to predict residual stress and deformation for an L-PBF build part. It was found that a line-heating model is not suitable for analyzing a large L-PBF built part. The layer heating method is a potential method for analyzing a large L-PBF built part. The experiment was conducted to validate the model predictions.

Keywords Additive manufacturing · Laser powder bed fusion · Finite element analysis · Residual stress · distortion

1 Introduction

Laser powder bed fusion is used to build three-dimensional products using a layer-by-layer approach. Typical L-PBF built parts, like most additive manufactured parts, are complex in shape and are destined to become more complex as engineers fine tune the art of design for AM. This complexity of shape creates a challenge for defects, microstructure, residual stress, and deformation control within the part. Melt pool

dimension control, microstructure control, residual stress, and deformation control are needed to build geometries accurately and have good mechanical properties. Therefore, AM process control requires the ability to predict melt pool dimensions, solidification microstructure, residual stress, and deformation during and before processing.

The highly localized heating and repeated thermal cycles that are characteristic of this process induce complicated microstructure distributions in the consolidated part. The residual stresses resulting from cyclic thermal expansions and contractions induce distortion in the component, which can negatively impact overall part quality. Many computational models have been developed to study the evolution of temperature, microstructure, stress, and distortion in L-PBF [1]. However, most of these models only simulate a small part of the problem with a fine mesh, or solve the entire problem using a coarse mesh to avoid long computational times. Studies focused on accurately predicting distortion of full-sized L-PBF parts have been limited.

✉ Y. P. Yang
yyang@ewi.org

M. Jamshidinia
mahdi.jamshidinia@gmail.com

P. Boulware
pboulware@ewi.org

S. M. Kelly
smkellyvt@gmail.com

¹ EWI, 1250 Arthur E. Adams Drive, Columbus, OH 43221, USA

Microstructural models [2–7] were developed to achieve the control of microstructure by tailoring the AM machine parameters. Modeling and validation of a solidification microstructure can be leveraged to reduce iteration cost in obtaining a desired microstructure. Kelly [2] developed a thermal and microstructural model for multilayered Ti-6Al-4V deposits in the laser metal deposition process. The microstructure model predicted the alpha phase fraction to quantify the effect of thermal cycling on the as-deposited microstructure evolution. Alpha dissolution and growth were modeled assuming one-dimensional plate dissolution according to a parabolic rate law and a Johnson–Mehl–Avrami–Kolmogorov (JMAK) nucleation and growth model, respectively. Following Kelly’s work, Irwin et al. [3] developed a Ti-6Al-4V microstructural model to calculate the phase fractions, morphology, and alpha lath width for a measured or modeled thermal history. Evolution of alpha lath width is calculated using an Arrhenius equation. Vastola et al. [4] implemented the non-equilibrium equations for phase formation and dissolution in AM modeling framework. The model was developed for the Ti6Al4V alloy and studied the microstructure evolution during selective laser melting process. Recently, Smith et al. [5] provided an approach for incorporating thermodynamically consistent properties and microstructure evolution for non-equilibrium supercooling, as observed in additive manufacturing processes into finite element analysis. The predicted temperature response and microstructure evolution for additively manufactured stainless steel 316L using standard handbook-obtained thermodynamic properties are compared with the thermodynamic properties calculated using the CALculation of PHase Diagrams (CALPHAD) approach. Rodgers et al. [6] took the general Monte Carlo approach to predict three-dimensional grain structure in additively manufactured metals. Achary et al. [7] used computational fluid dynamics (CFD) analysis to predict melt pool characteristics and phase field modeling to simulate microstructure evolution in the as-deposited state for L-PBF process.

Many studies [8–19] have been conducted to investigate residual stress and deformation in L-PBF. An accurate estimation of residual stresses and distortion is necessary to achieve dimensional accuracy and prevent cracking and fatigue failure. Since many process variables affect AM, experimental measurements of residual stresses and distortion are time consuming and expensive. There are three types of models to predict residual stress and deformation during the additive manufacturing process. The first type of model is a three-dimensional, transient heat transfer and fluid flow model used to accurately calculate a transient temperature field for the residual stress and distortion modeling [8,9]. The second type of model is a thermomechanical model without modeling the fluid flow model. With this kind of model, Mercelis and Kruth [10] investigated the evolution

of residual stresses in L-PBF. Roberts et al. [11] and Hodge et al. [12] simulated the multilayer material deposition and demonstrated that local thermal histories were impacted by the processing of layers immediately above and resulted in multiple intervals of rapid heating and cooling. In order to enhance the computational efficiency of FEM, Nikoukar et al. [13] improved Cholesky algorithm by identifying discrete sparse bands and eliminating many zero multiplications in the lower triangular matrix to obtain the thermomechanical response much faster than currently available algorithms. Patil et al. [14] and Zeng et al. [15] developed an adaptive mesh technique to provide significant computational enhancements over other solution methodologies. The third type of model is a simplified model for large part simulation [16–19]. Papadakis et al. [18] proposed a volume-by-volume method in which three layers of materials were brought in to melt simultaneously. Denlinger et al. [19] developed a layer-by-layer coarsening strategy in which the lower layers of the finite elements were merged to maintain a low number of degrees of freedom in the model for the entire simulation. The effectiveness of the modeling strategy is demonstrated and experimentally validated on a large electron beam deposited Ti-6Al-4V part consisting of 107 deposition layers.

From the literature review of microstructural models for additive manufacturing processes, it can be seen that few models attempt to predict the microstructure and hardness for high-strength low-alloy (HSLA) steels built in L-PBF. From the literature review of various L-PBF numerical models for residual stress and distortion prediction, it was found that few models attempt to represent parts in the same length scales as those which are built in L-PBF because the numerical analyses are highly nonlinear and result in an expensive computational cost. This work attempted to develop a modeling method to predict microstructure and hardness for high-strength steels built with additive manufacturing processes and develop a generalized modeling method to predict residual stress and distortion on large built parts. The work was divided into two parts.

The Part 1 study extended a kinetics-based microstructural model which was originally developed to predict microstructure and hardness in a HAZ of a weld joint to simulate the microstructural evolution in L-PBF. More importantly, the tempering effect resulting from the following built layers on the resulted microstructural phases were modeled, which is the key to correctly predict the final hardness. It was also found that the top layers of a built part have a higher hardness because of the lack of the tempering effect. An experiment was conducted to build a sample and then measure hardness. The measured hardness agreed with the model predictions. This study was conducted on high-strength steel 4140.

The Part 2 study has developed and validated several numerical models including moving heat-source model, a line heating model, and a layer heating model to predict resid-

ual stress and distortion on a bridge sample. A sequentially coupled thermal and mechanical analysis method was developed to predict residual stress and deformation for L-PBF build part. It was found that both the moving heat-source model and the line heating model are not suitable for analyzing a large L-PBF built part. It has been concluded that a layer-heating method could be an efficient modeling technique to predict distortion in full-sized L-PBF parts. The predicted deformation from the layer-heating method was validated by experimental data. This study was conducted on Inconel 718.

The computational methods used in this paper are given in Sect. 2 including governing equations, boundary conditions, heat source models, a microstructure model, a tempering model, etc. Section 3 presents the experimental work which includes hardness measurement and deformation measurement. Section 4 discusses the results of microstructure and hardness predictions and validations. Section 5 introduces the analysis results of residual stress and deformation with two computation models: a line-heating model and a layer-heating model.

2 Computational methods

Heat energy is transferred and dissipated in four main modes: reflection, conduction, convection, and radiation when a laser beam hits the powder bed surface in L-PBF. Since metallic materials are lustrous in nature, a large part of the incident energy is reflected. Absorptivity depends on the material and powder morphology. Heat energy absorbed in the powder is subsequently conducted through surrounding regions: solidified part, base plate, and powder bed. The ambient environment in L-PBF included an inert gas such as argon or nitrogen, which results in heat loss due to convection. Heat energy losses due to radiation also occur during L-PBF processing. Heat reflection, conduction, and convection are modeled in this work. The radiation effect was not explicitly modeled in this work since its influence is much smaller compared to other forms of heat loss [20]. The radiation effect was considered by increasing the heat convection coefficient slightly.

2.1 Governing equation and boundary conditions

For a typical L-PBF machine, fabrication takes place inside a closed build chamber purged using an inert gas. The heat transfer process can be described by governing Eq. (1)

$$\rho C_p \frac{\partial T}{\partial t} = \nabla \cdot (k \nabla T) + Q \tag{1}$$

where ρ is the mass density, C_p is the constant-pressure specific heat, T is the temperature field, t is time, k is the temperature-dependent thermal conductivity, Q is the volumetric internal heat generation rate which will be discussed in the section of heat-source models.

The base plate is preheated to a certain temperature (T_0) prior to fabrication, which is described in Eq. (2) as initial condition of the problem.

$$T(x, y, z, 0) = T_0 \tag{2}$$

Heat convection between the solidified part, powder, and the surrounding environment is described using Eq. (3)

$$-k(T) \frac{\partial T}{\partial z} = h(T - T_e) \tag{3}$$

where h is the convective heat transfer coefficient and T_e is the surrounding-environment temperature.

The thermal history dependent quasi-static mechanical analysis is performed to obtain the mechanical response of the workpiece during the deposition. The results of the thermal analysis are loaded into the mechanical analysis. Elastic-plastic material model with isotropic hardening was used in this work. Implicit analyses were conducted to predict strain, stress, and deformation. The governing stress equilibrium equation is

$$\nabla \cdot \sigma = 0 \tag{4}$$

where σ is the stress.

The mechanical constitutive law is

$$\sigma = C \varepsilon_e \tag{5}$$

$$\varepsilon = \varepsilon_e + \varepsilon_p + \varepsilon_T \tag{6}$$

where C is the fourth order material stiffness tensor, and ε , ε_e , ε_p , and ε_T are the total strain, elastic strain, plastic strain, and thermal strain, respectively. Material melting was modeled by setting stress and strain to zero when the temperature reaches to the material melting temperature.

The mechanical boundary condition was to fix the base-plate bottom during L-PBF processing. After cooling down, the built part was disconnected from the base plate to check for final deformation by removing a layer of elements.

2.2 Heat source models

Accurately simulating the transient temperature field in L-PBF is vital for determining the thermal stress distribution and residual stress states in built parts. The modeling of the problem involving multiple layers is equally of great importance because the thermal interactions of successive

layers affect the temperature gradients, which govern the heat transfer, microstructure, and thermal stress development mechanisms. Most of the current heat source models originate from welding simulations [21] because the fundamental physics of the welding process are similar to those seen in AM processes for a single pass.

2.2.1 Double-ellipsoidal heat-source model

A moving heat-source model developed on the ABAQUS finite element software [22] for welding simulation was used to predict temperature evolution during L-PBF processing. The heat-source model was developed based on the Goldak double ellipsoidal model [23], as shown in Eq. (7).

$$q(x, y, z, t) = f \frac{6\sqrt{3}P\eta}{abc\pi\sqrt{\pi}} e^{-\frac{3x^2}{a^2}} e^{-\frac{3y^2}{b^2}} e^{-\frac{3[z+v(t-t_0)]^2}{c^2}} \quad (7)$$

where q is the calculated heat flux as a function of location and time, f is a factor, η is arc efficiency, P is laser power, and v is laser travel speed. a , b , and c are the semi-axes of the ellipsoid which were defined based on the hatch distance.

The double ellipsoidal heat-source model has been used extensively to model heat sources including lasers and electron beams in AM. To accurately model the motion of the heat source, the simulation time increments must be small enough so that the source moves a distance smaller than its radius over the course of each increment. When the source radius is small and its velocity is large, a strict condition is imposed on the size of time increments regardless of any stability criteria. In the L-PBF process, where radii of 0.1 mm and velocities of 900 mm/s are typical, a significant computational burden can result. Therefore, a line heat-source model was developed to relieve this burden by averaging the heat source over its path.

2.2.2 Line heat-source model

Since the laser in the L-PBF process is moving so fast, each laser-scanned line is visualized as a line heated at one time. Thus, the line-heating method was developed to model this phenomenon by integrating the Goldak heat source model in the time taken to heat a line [24]. This model allows the simulation of an entire heat source scan in just one time increment, which makes the accurate modeling of powder bed processes more computationally efficient. The equation used to calculate a heat flux for a heat line can be expressed as follows:

$$Q(x, y, z, t) = \int_{t_0}^{t_0+\Delta t} q(x, y, z, t) dt$$

$$Q(x, y, z, t) = \frac{3P\eta}{\Delta t v ab \pi} \exp\left(-\frac{3x^2}{a^2} - \frac{3y^2}{b^2}\right) \operatorname{erf}\left(\frac{\sqrt{3}(z+vt)}{c}\right) \Big|_{t=t_0}^{t_0+\Delta t} \quad (8)$$

where t_0 is the time at the beginning of the increment and Δt is the time increment. This formulation allows time increments to be made arbitrarily large, without skipping any elements as Goldak's model does.

The line heating model can increase the analysis speed but has some limitations. The line heating model cannot simulate the transient phenomena during laser traveling such as melting-pool dynamics. The laser turning around to move to another heating line cannot be modeled either. These details are less important to predict distortion on the built part [24].

2.2.3 Layer heating model

A lump-pass modeling method was developed in the welding simulation [25] to reduce the computational time in which several weld passes were lumped together and heated to melting temperature in a short time. This method was extended to model AM processes named as layer-heating modeling method.

The layer-heating modeling method can greatly reduce the computation time in simulating a part built in L-PBF in which several layers of materials were brought into their melting temperature in a short time. This modeling method can be conducted in a coarse mesh so that the computational time can be further reduced for modeling a large built part.

The layer-heating model further simplifies the physics in L-PBF. Therefore, many phenomena occurred in a heating line and a heating layer in the L-PBF cannot be modeled. To overcome this problem, a new modeling method, local to global approach, is under development. In the local models, the detail phenomena are modeled. Then the local-model results are mapped into a global model to predict residual stress and distortion.

2.3 Microstructure model

Ashby, Easterling, and Ion proposed a kinetics-based model [26,27] for the prediction of microstructure in the HAZ of a fusion-welded joint. This model has been widely used to predict the microstructure and hardness in a weld joint by inputting material chemical compositions and temperature history. In this study, a stand-alone python script was developed for predicting microstructure and hardness of steels for AM. The script can be used to predict the distribution of each individual phase such as ferrite, bainite, and martensite and the hardness map in the built area by coupling with the

thermal model. The calculation of microstructure starts by calculating the carbon equivalent (CE) using Eq. (9).

$$CE = C + \frac{Mn}{6} + \frac{Cr + Mo + V}{5} + \frac{Ni + Cu}{15} \quad (9)$$

where C is carbon, Mn is manganese, Cr is chromium, Mo is molybdenum, V is vanadium, Ni is nickel, and Cu is copper. All composition elements are defined in weight percent.

The CE can be used to relate to the following critical cooling rates:

$$\begin{aligned} \log \Delta t_{1/2}^m &= 8.79CE - 1.52 \\ \log \Delta t_{1/2}^b &= 8.84CE - 0.74 \end{aligned} \quad (10)$$

where $\Delta t_{1/2}^m$ is the critical time that gives a 50% martensite and 50% bainite structure, and $\Delta t_{1/2}^b$ is the time that gives a 50% mixture of bainite and 50% ferrite structure. From the critical cooling rate, the final volume fraction of martensite (V_m), bainite (V_b), and perlite plus ferrite (V_{fp}) can be calculated from the following equations [11]:

$$\begin{aligned} V_m &= V_{\max} \exp \left\{ -0.69 \left(\frac{\Delta t}{\Delta t_{1/2}^m} \right)^2 \right\} \\ V_b &= V_{\max} \exp \left\{ -0.69 \left(\frac{\Delta t}{\Delta t_{1/2}^b} \right)^2 \right\} - V_m \\ V_{fp} &= 1 - (V_m + V_b) \end{aligned} \quad (11)$$

where Δt is the transformation time and V_{\max} is the maximum volume fraction of austenite which can form during a thermal cycle with a peak T and be calculated using the following equations:

$$\begin{aligned} V_{\max} &= 0 && \text{if } T_p \leq A_1 \\ V_{\max} &= \frac{T_p - A_1}{A_3 - A_1} + \frac{C}{0.83} \frac{A_3 - T_p}{A_3 - A_1} && \text{if } A_1 < T_p < A_3 \\ V_{\max} &= 1 && \text{if } T_p > A_3 \end{aligned} \quad (12)$$

where A_1 (K) and A_3 (K) can be estimated by the following equations:

$$\begin{aligned} A_1 &= 1187.8 + 9780.3C && \text{if } C \leq 0.019 \\ A_1 &= 999.78 && \text{if } C > 0.019 \\ A_3 &= 937.1 + 250.91 \exp(-1.6636C) && \text{if } C \leq 0.76 \\ A_3 &= 999.78 && \text{if } C > 0.76 \end{aligned} \quad (13)$$

The hardness for alloy steels can be calculated using the following empirical equation [27].

$$H_m = 127 + 949C + 27Si + 11Mn + 8Ni$$

$$+ 16Cr + 21 \log CR$$

$$\begin{aligned} H_b &= -323 + 185C + 330Si + 153Mn + 65Ni \\ &+ 144Cr + 191Mo + (89 + 53C - 55Si - 22Mn \\ &- 10Ni - 20Cr - 33Mo) \log CR \end{aligned}$$

$$\begin{aligned} H_{fp} &= 42 + 223C + 53Si + 30Mn + 12.6Ni + 7Cr + 19Mo \\ &+ (10 - 19Si + 4Ni + 8Cr - 130V) \log CR \end{aligned} \quad (14)$$

where H_m , H_b , and H_{fp} are the hardness of martensite, bainite, and perlite plus ferrite, respectively. CR is the cooling rate at 700 °C (°C/h). The final hardness (H) at each point of the weld can be estimated using the rule of mixtures.

$$H = H_m V_m + H_b V_b + H_{fp} V_{fp} \quad (15)$$

Based on the steel chemistry input by the user and the cooling rate calculated from the thermal analysis, Eqs. (9) through (15) predict the final volume fractions and hardness.

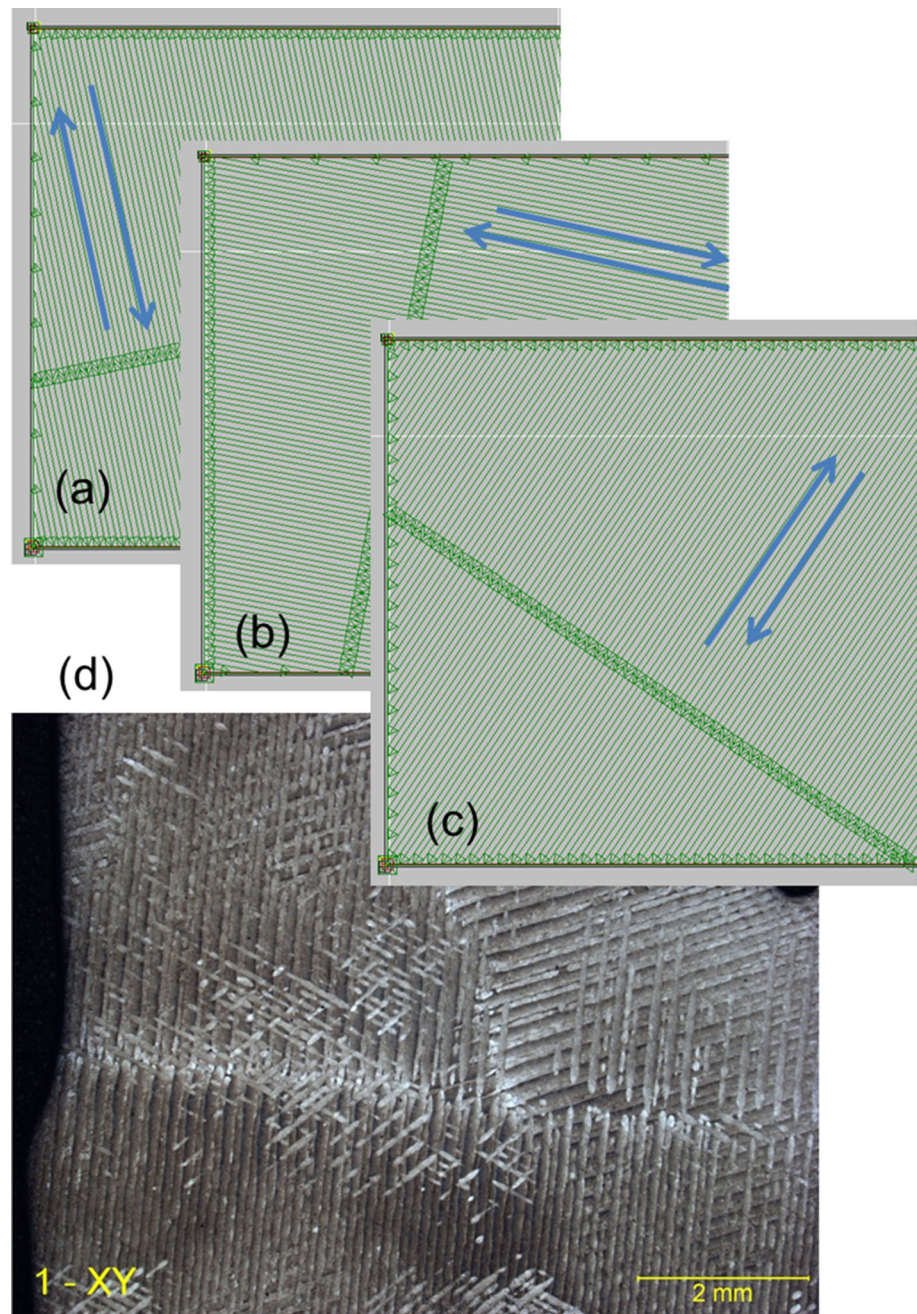
2.4 Tempering model

Since L-PBF is a process to build a part by many layers. The following layers will have a tempering effect on the previous built layers. The tempering effect has a great influence on the hardness of the resulted microstructure. Grange et al. [28] studied the tempering temperature effect on the hardness of martensite microstructure and created a diagram to show the relationship between carbon weight percentage, tempering temperature, and hardness. Based on the diagram, the Vickers hardness of martensite is about 720 HV for a steel containing 0.42% of carbon without tempering or tempering at a lower temperature. By tempering at a temperature of 315.5°C, a much lower hardness (Vickers hardness, 440 HV) can be obtained. To model the tempering effect on the hardness of the built part, a tempering model was developed based on the relationship between chemical compositions, tempering temperature, and hardness. The model inputs are the percentage of carbon and the tempering temperature. The average peak temperature in the following layers was used as the tempering temperature in the developed code.

2.5 Creation of layers and heating lines

A Fortran program was developed to slice an imported part into layers automatically based on an input layer thickness. For each layer, heating lines are automatically created according to the L-PBF process parameters (stripe width and hatch distance). The heating lines were rotated layer by layer with an angle of 67°. Figure 1 illustrates the created heating lines and the surface observation in a built part.

Fig. 1 Created heating lines and the surface macrograph in a built part. **a** Layer n ; **b** Layer $n + 1$; **c** Layer $n + 2$; **d** Surface macrograph



2.6 Model the material switching from powder to solid

A program modeling material ID switching from powder to solid was developed in this study. A similar approach has been used by other researchers [29,30] to model the transition from fresh powder to dense solid. The material ID switch is based on the laser-heat source location. Figure 2 shows the laser location and material ID side by side and one at a time on a 2.5 by 2.5 mm built block. In Fig. 2a, gray color shows

the melt pool which is the laser location. In Fig. 2b, the red color represents solid material and blue color represents the powder. The base plate is also represented using the blue color.

2.7 Strategy for modeling AM processes

Microstructure and hardness are determined by chemical compositions and thermal history. Thermal history depends on a local geometry, heat convection, and radiation. There-

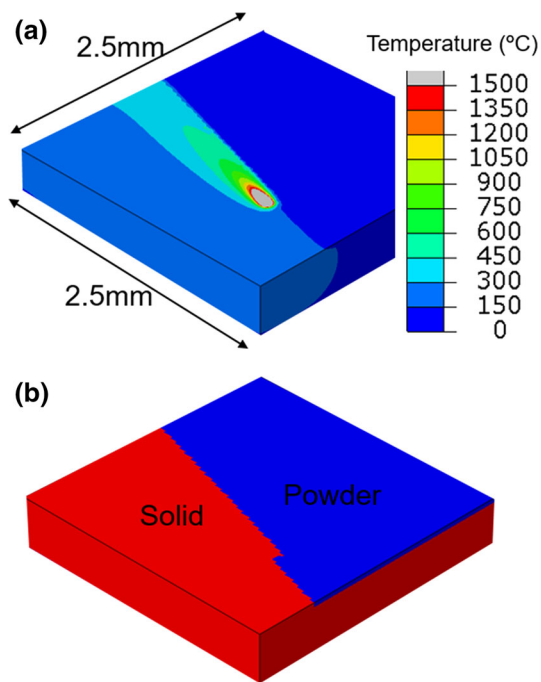


Fig. 2 Model material ID switching from powder to solid (background blue color is the base plate). **a** Predicted temperature; **b** Material ID with red color for solid and blue color for powder

fore, microstructure and hardness can be predicted by simulating the building process in a local interested volume without modeling an entire part. This strategy allows the detailed temperature history during AM processes to be modeled using the double ellipsoidal heat source model discussed above in multiple local models. Each local model is run separately to understand the microstructure and hardness in an interested location. A sequential coupled thermal and metallurgical analysis can be used to predict microstructure and hardness in local models.

Residual stress and distortion are related to structure stiffness which is determined by geometry. Therefore, residual stress and distortion must be predicted in a global model including the entire geometry. Because of extreme long computation time, the line-heat source model and the layer-heating model discussed above will be used in this study. A sequential couple thermal and mechanical analysis can be conducted to predict residual stress and distortion.

If microstructure, residual stress, and distortion are all of interest, multiscale modeling approach [29] would be used in which local models are used to predict microstructure and hardness and a global model is used to predict residual stress and distortion. A coupled thermal, metallurgical, and mechanical analysis can be conducted to predict microstructure, residual stress, and distortion in a built part. This will be the future direction for this study.

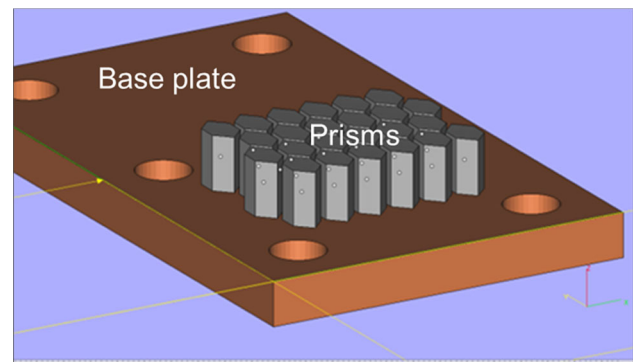


Fig. 3 Hexagonal prisms ($12 \times 12 \times 10$ mm) were built for screening process parameters

3 Experimental work

Experiments were conducted to validate the predicted hardness by sequentially coupled thermal and metallurgical analysis and the predicted deformation by sequentially coupled thermal and mechanical analysis. Test samples were built with L-PBF in an EOS M280 machine which has a 400 W laser.

3.1 Hardness measurement

Hexagonal prisms ($12 \times 12 \times 10$ mm), as shown in Fig. 3, were built with 4140 steel powder using L-PBF process with the parameters shown in Table 1. The steel powder chemical compositions are shown in Table 2. Macrographs were prepared by cutting the prisms along the height, as shown in Fig. 4. Vickers hardness was measured with a load 0.5 kgf along the height direction, as indicated with a red line in Fig. 4.

3.2 Deformation measurement

A bridge sample, as shown in Fig. 5, was built using L-PBF process with the process parameters shown in Table 3. The stripe overlap was 0.08 mm and layer neat thickness was 0.04 mm. The material was Inconel 718.

4 Predictions of microstructure and hardness

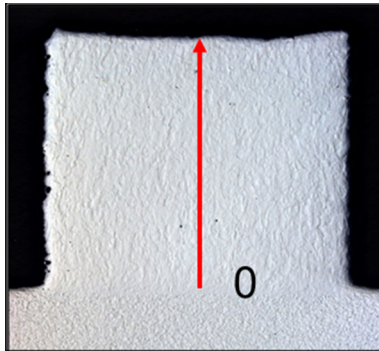
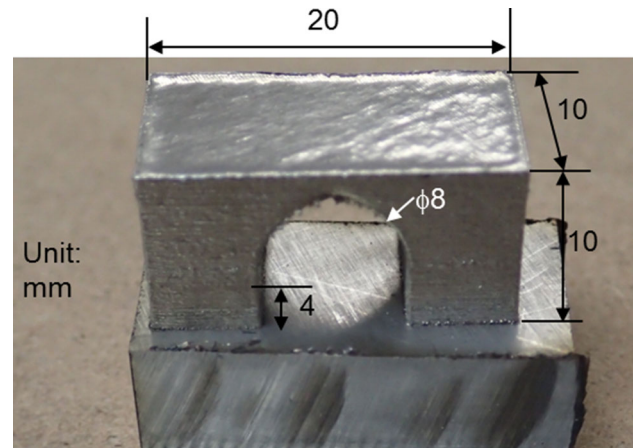
Since microstructure is mainly controlled by a local temperature history, a small block with a dimension of 2.5 by 2.5 mm was built for the temperature and microstructure prediction. The following sections introduced the predicted temperature, microstructure, and hardness distributions on an L-PBF built block with 4140 steel powder.

Table 1 Parameters for L-PBF process

Parameter set	Laser power (W)	Scan speed (mm/s)	Hatch distance (μm)	Stripe width (mm)
EXP-03	350	867	90	10

Table 2 Chemistry (wt%) of the 4140 powder

C	Mn	P	S	Si	Cr	Mo	Fe	N	O
0.44	0.90	< 0.01	< 0.02	0.21	1.00	0.21	bal	0.03	0.02

**Fig. 4** Vickers hardness was measured along the red line from the bottom to the top of a built sample**Fig. 5** A bridge sample built with L-PBF process to collect deformation

4.1 Temperature history prediction

Thermal analyses were conducted by inputting the material properties listed in Table 4 with the Goldak double ellipsoidal heat-source model discussed in Sect. 2.2.1 to predict the temperature history. Heat loss due to convection and radiation was modeled. Figure 6 shows the predicted temperature for the first 10 layers at a time. The gray color shows the predicted melt pool. The heat source was moving on the surface based on the defined tool path. Each layer has about 60 heat lines. The figure just shows the temperature distributions during heating one line. The temperature distributions in the layers show the rotation of heating path as the layers were built up.

The temperatures for all points in the model as a function of location and time were predicted and saved to a database for microstructure and hardness prediction. Figure 7 shows the predicted temperature histories at the points shown in Fig. 7a. Temperature history at a point in layer 2, layer 4, and layer 6 were plotted, as shown in Fig. 7b–d, respectively. Heating and cooling of each point was repeatedly experienced. The peak temperature became lower and lower as the more layers were built. This is because the distance of built layers to the plotted point become farther away as the layers are built up.

4.2 Microstructure prediction

Final microstructure was predicted by inputting the chemical compositions in Table 2 and the temperature history shown in Fig. 8. Figure 8a is the re-plot of layer 2 temperature shown in Fig. 7b. It can be found that the first temperature peak (marked as layer 2 in Fig. 8a) contains two peaks inside, as shown in Fig. 8c, and the second temperature peak (marked as layer 3 in Fig. 8a) contains three peaks inside, as shown in Fig. 8b. Similarly, the fifth temperature peak (marked as layer 6 in Fig. 8a) contains three small peaks inside, as shown in Fig. 8d.

Figure 8b, c show that four temperature peaks are higher or close to 1400°C . This means that this point experienced repeated melting during the L-PBF process. The final melting (P4) determines the final microstructure at this point. Therefore, the microstructure code uses the temperature history to predict the microstructure at this point. Almost 100% martensite was predicted in the build, as shown in Fig. 9. To verify the microstructure prediction, commercial software JMatPro [32] was used to predict the microstructure of AISI 4140, as shown in Fig. 10. Based on the continuous cooling transformation (CCT) diagrams, 100% martensite will be formed if

Table 3 Parameters for L-PBF process

Sample	Laser power (W)	Scan speed (mm/s)	Hatch distance (mm)	Stripe width (mm)
Bridge	285	960	0.1	10

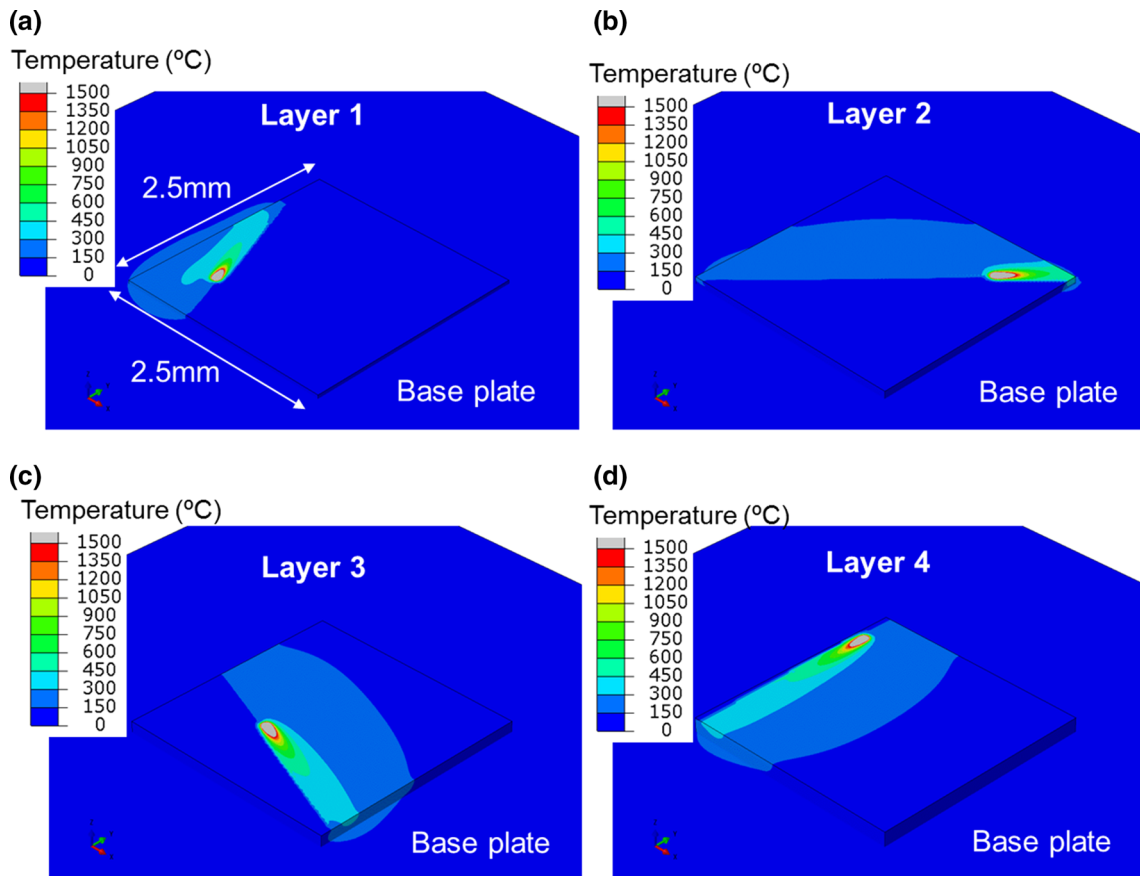


Fig. 6 Predicted temperature evolution. **a** on the layer 1; **b** on the layer 2; **c** on the layer 3; **d** on the layer 4

Table 4 Thermal-physical properties of 4140 steel [31]

Density (g/cm ³)	7.85
Thermal conductivity (W/m/°C)	43
Specific heat (J/kg/°C)	477
Latent heat of fusion (J/kg)	220,000

the cooling rate is higher than 100°C/s. The cooling rate in the L-PBF is much higher than 100°C/s. Therefore, 100% martensite was formed in the build of L-PBF.

4.3 Hardness prediction

Based on the predicted microstructure (Fig. 9), hardness was predicted using Eq. 9 and the tempering model. It is important that the tempering effect was modeled since L-PBF includes

many layers to build a structure. The later layers have a tempering effect on the previous layers. The inputs to the tempering model discussed in Sect. 2.3 are a tempering temperature and chemical compositions.

The tempering temperature for each point in the model was calculated by averaging the peak temperatures resulted from depositing later layers. For example, Fig. 7b shows that the tempering temperature for a point in layer 2 is 315°C. The carbon weight percentage is 0.44. Therefore, the resulted hardness is 440 HV based on the relationship between tempering temperature, carbon weight percentage, and hardness, as shown in Fig. 1. Similarly, the hardness for all points was calculated, as shown in Fig. 11. The green color in Fig. 11 shows the reduced hardness with tempering effect. The final layers had a high hardness because of no tempering effect. The average Vickers hardness in the green color range is about 460 HV.

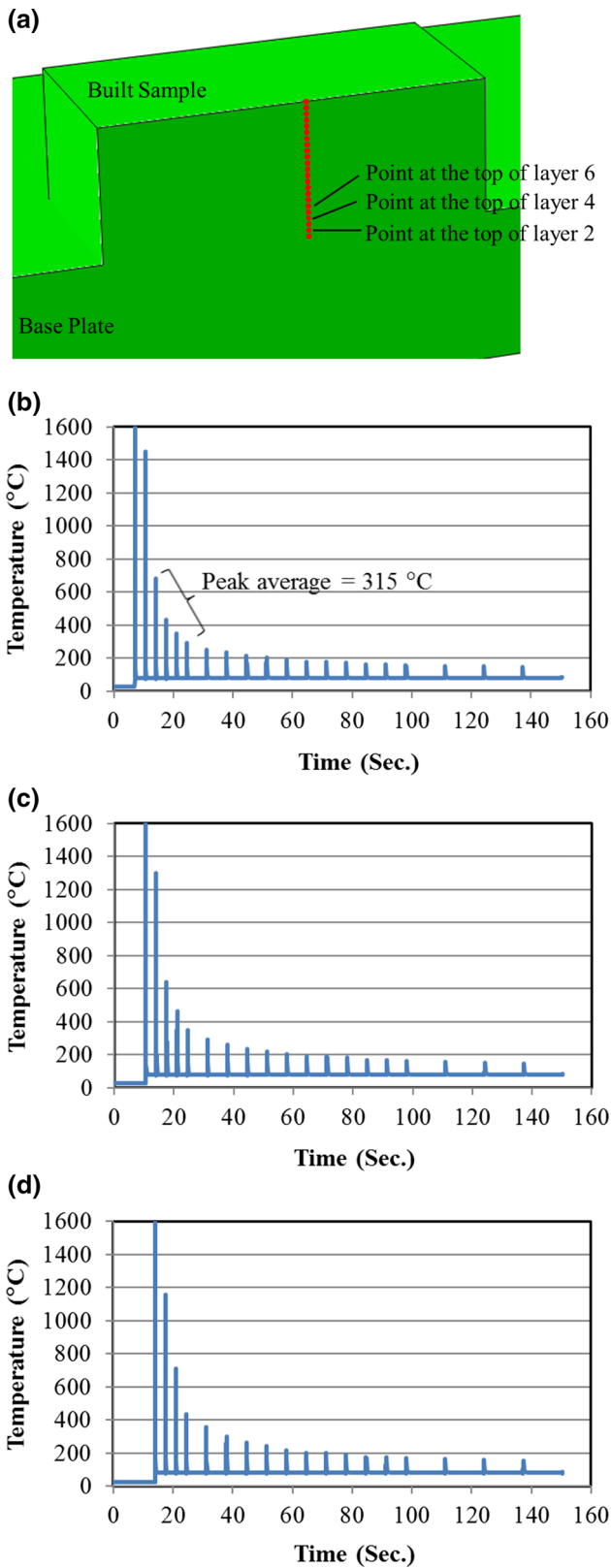


Fig. 7 Predicted thermal cycles for layers 2, 4, and 6. **a** Point locations for plotting thermal histories; **b** Temperature history for the point on the top of layer 2; **c** Temperature history for the point on the top of layer 4; **d** Temperature history for the point on the top of layer 6

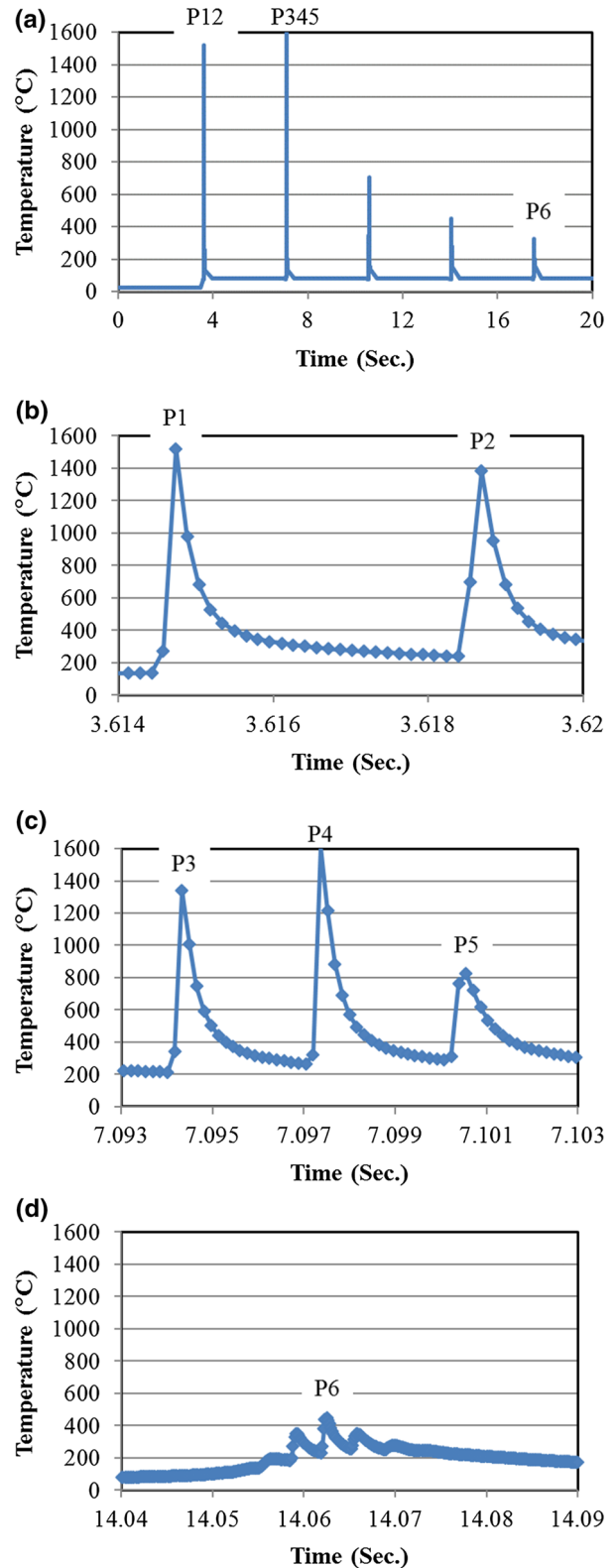


Fig. 8 Replotted temperature history for the point on the top of layer 2 (one large peak including 2–3 peaks inside). **a** Temperature history for the first 20 seconds which includes temperature peaks P12, P345, and P6; **b** Replot the temperature peak P12 with reduced time scale; **c** Re-plot the temperature peak P345 with reduced time scale; **d** Re-plot the temperature peak P6 with a reduced time scale

Fig. 9 Predicted martensite distributions in the simulated block

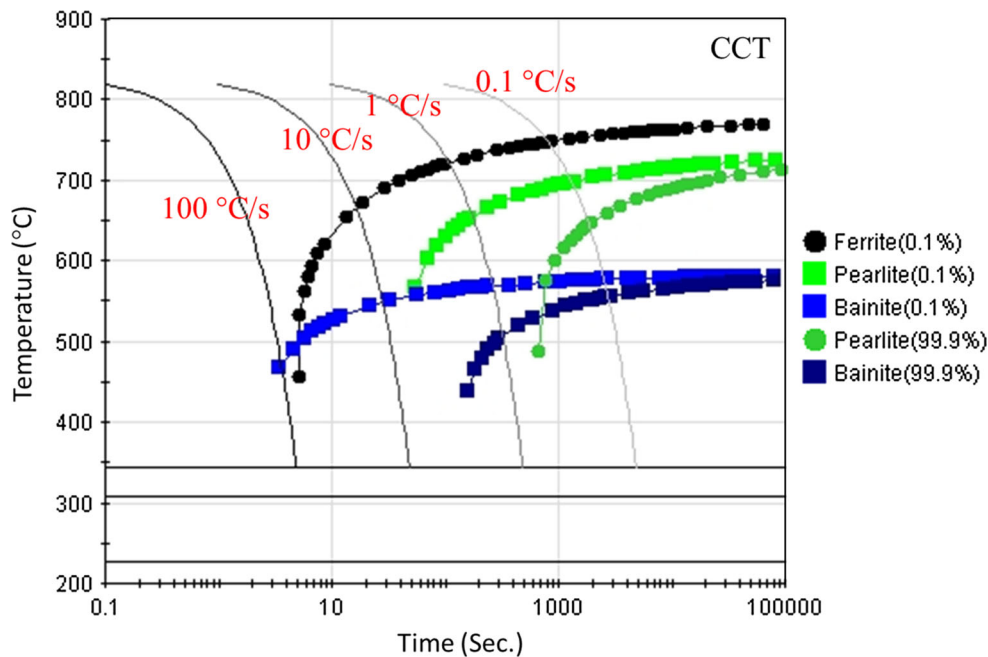
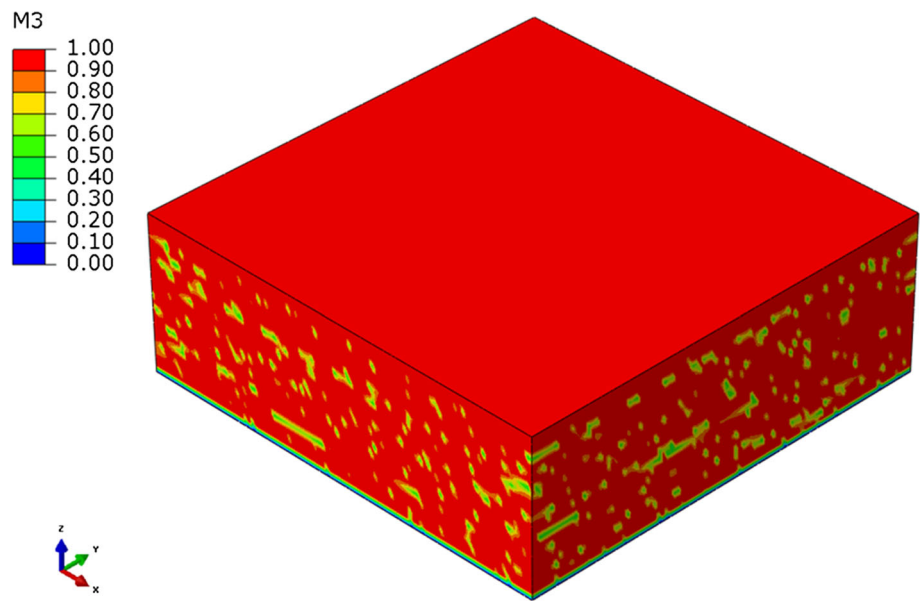


Fig. 10 Microstructure predictions using JMatPro software [32] based on cooling rate and chemical compositions

4.4 Experimental validation

To validate the hardness prediction as shown in Fig. 11, Vickers hardness was measured along the centerline of three built prisms discussed in Sect. 3.1, as shown Fig. 12. Figure 12 shows the similar trend as model predicted hardness distributions in Fig. 11. The last few layers have a much higher hardness than the lower layers.

5 Predictions of residual stress and deformation

The second goal of this study is to develop a modeling method to predict distortion in a large built part with L-PBF. Inconel 718 was used for this study. Sequential thermal and mechanical analyses were conducted on the bridge sample discussed in Sect. 3.2 with both the line-heating model discussed in Sect. 2.2.1 and the layer-heating model discussed

Fig. 11 Predicted Vickers Hardness with modeling the tempering of martensite. **a** Full-model view; **b** half-model view

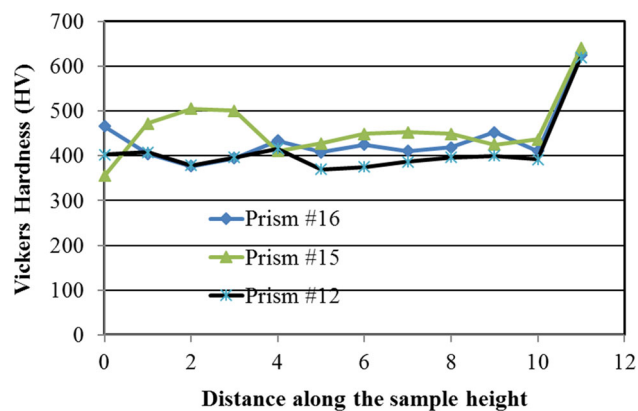
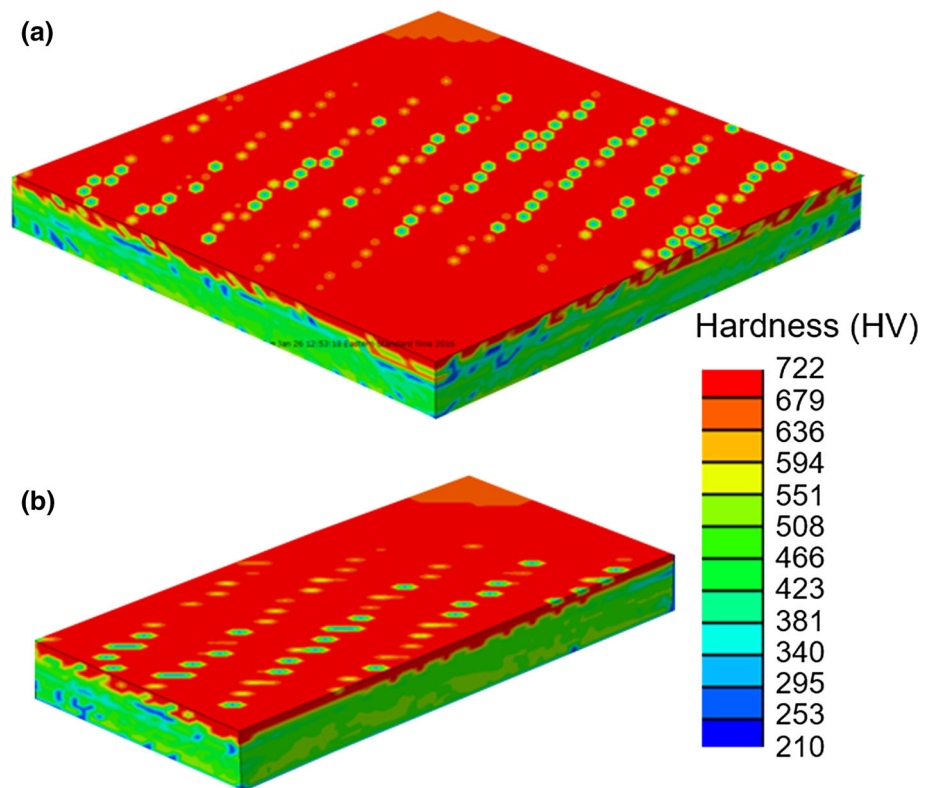


Fig. 12 Hardness measurement along the height of built prisms

in Sect. 2.2.3 to find out if they are suitable for predicting residual stress and deformation in a layer part.

5.1 Finite element model

A finite element model, as shown in Fig. 13, was built for the bridge sample discussed in Sect. 3.2 by considering the layer thickness 0.04 mm, hatch distance 0.1 mm, and laser heating spot radius 0.1 mm. To limit the model size, only one element was planned in one layer, in one hatch distance, in one laser heating spot. Even with this large mesh size, about

3.76 million nodes and 3.66 million elements were created in the model. It will be difficult to solve this problem with a moving heat source model as discussed in Sect. 2.2.1. The computational time will be too long for a moving heat-source, thermal-elastic-plastic analysis.

Heating lines were automatically created with the computer program discussed in Sect. 2.4. Figure 14 shows the created heating lines in the selected five layers for illustrating the number of heating lines per layer. To build the bridge sample, 250 layers are needed. The top layer included 368 heating lines. For so many heating lines, it is impracticable to model and execute a transient thermos-mechanical simulation without appropriate simplifications.

5.2 Material properties

Sequentially coupled thermal and mechanical analysis requires temperature dependent material properties. Tables 5, 6, 7, 8 show the temperature dependent thermal conductivity, coefficient of thermal expansion, Young's modulus, and Poisson's ratio of Inconel 718, respectively [33]. Temperature dependent special heat of Inconel 718 cannot be found. A constant value, 435 J/kg °C, was used. The solidus and liquidus temperatures of Inconel 718 are 1260 and 1336 °C, respectively.

Fig. 13 A finite element model for the built bridge sample

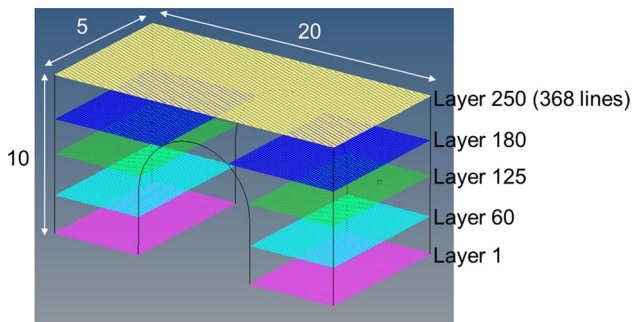
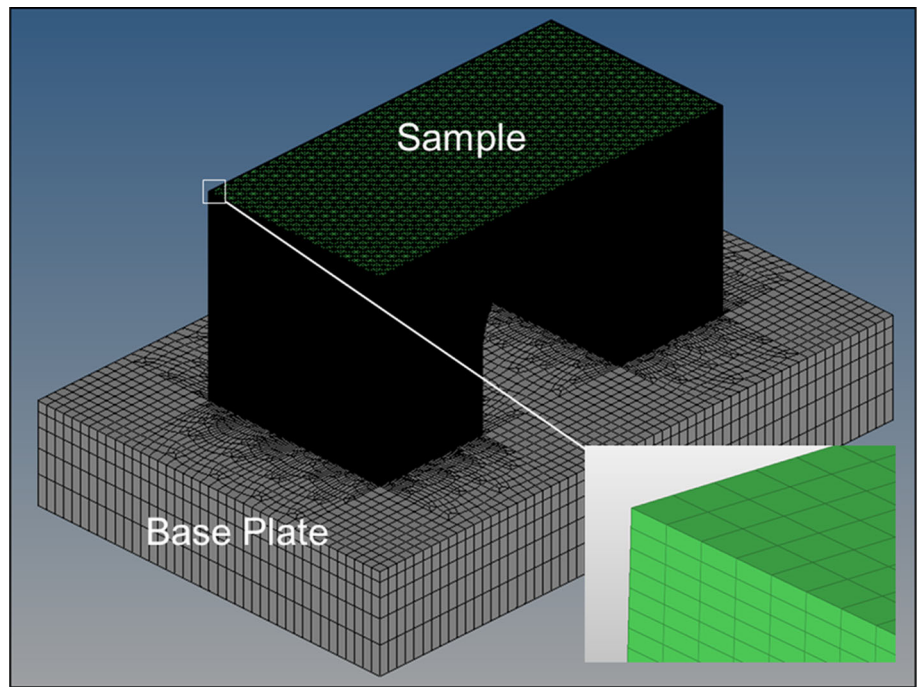


Fig. 14 Heat lines for built layers

5.3 Prediction with line-heating model

To reduce the computational time for modeling L-PBF, the line-heating method discussed in Sect. 2.2.1 was evaluated at first on a part of the bridge-sample model. Figure 15 shows the predicted temperature distributions with the line-heating model at a time. The gray color line shows the melting zone. The heating line is moving from the back corner to the front corner. As the line is moving, the temperature behind the heating line is reducing.

Figure 16 shows the predicted maximum principal stress distributions in a block model. Tensile stresses are predicted on the outer surface and compressive stresses are predicted inside the block, which explains why cracks that initiate on the surface stop propagating a certain depth during L-PBF with some crack-sensitive materials.

Table 5 Thermal conductivity of Inconel 718

Temperature (°C)	Thermal conductivity (W/m °C)
21	11
93	13
204	14
316	16
427	18
538	20
649	22
760	23
871	25
982	27
1093	29

Table 6 Coefficient of thermal expansion of Inconel 718

Temperature (°C)	Coefficient of thermal expansion (mm/mm °C)
93	1.32E-05
204	1.36E-05
316	1.39E-05
427	1.43E-05
538	1.46E-05
649	1.51E-05
760	1.60E-05

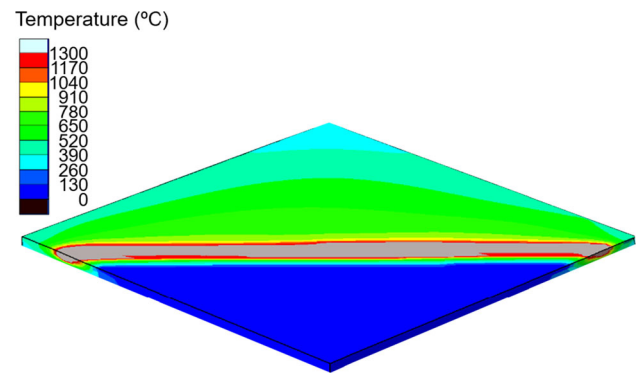
Table 7 Young's modulus of Inconel 718

Temperature (°C)	Young modulus (MPa)	Poisson's ratio
21	199,955	0.29
38	198,576	0.29
93	195,818	0.29
149	193,060	0.28
204	190,302	0.28
260	186,855	0.28
316	184,097	0.27
371	180,649	0.27
427	177,891	0.27
482	174,444	0.27
538	170,996	0.27
593	166,859	0.28
649	163,412	0.28
704	158,585	0.29
760	153,759	0.31
816	146,864	0.32
871	139,279	0.33
927	129,626	0.33
982	119,973	0.34
1038	109,631	0.37
1093	98,599	0.40

Table 8 Yield strength of Inconel 718

Temperature (°C)	Yield strength (MPa)
16	1209
87	1164
200	1120
308	1089
421	1065
537	1067
648	1023
710	969
757	875
817	543
882	306
990	134
1093	74

It took a week to have a solution for the simulated block. For a large built part, the computation will be much longer. Therefore, the line-heating model cannot be used to simulate the L-PBF with today computation power.

**Fig. 15** Predicted temperature distributions with the line-heating model

5.4 Prediction with layer-heating model

Three built layers were lumped into one layer in the layer-heating model and heated to melting temperature in a short time. The time depends on the process parameters and material properties. There are three numerical steps for one layer: depositing a layer, heating the layer, and cooling down. This three-step approach was repeated for all layers. It took 9.1 h to get one complete solution including a thermal analysis to predict temperature and a mechanical analysis to prediction distortion.

It should be pointed out that the laser scan direction and scan path within each layer cannot be considered in this simplified modeling approach. These two factors may have small effects on distortion prediction which will be studied in a future project.

Figure 17 shows predicted temperature distributions on the bridge sample after heating one layer to material melting temperature. A high temperature gradient was formed near the heating layer, which is critical to predict the deformation correctly. Figure 18 shows the predicted deformation shape and vertical deformation magnitudes. Because of the shrinkage of built materials, the sample was bent down in the middle. Note that the deformation was magnified by five times for better visualizing the deformation shape.

5.5 Experimental validation

To validate the predicted deformation shape and magnitudes, the bridge sample was cut off from the substrate with wire electrical discharge machining method (EDM). Figure 19 shows the deformation shape of the bridge sample. To highlight the deformation shape, a grid (0.59 by 0.59 mm) was laid on the part. It can be observed that the top surface of the bridge was bent down in the middle. To make a quantitative comparison, the deformation magnitudes on the top surface of the bridge sample were compared, as shown in Fig. 20. The

Fig. 16 Predicted maximum principal residual stress in a built block

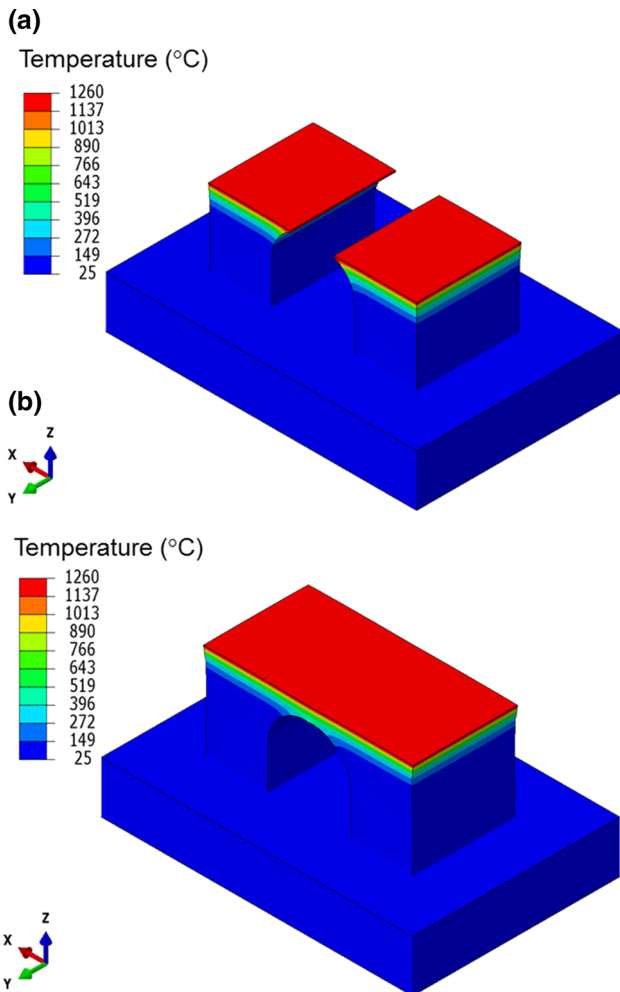
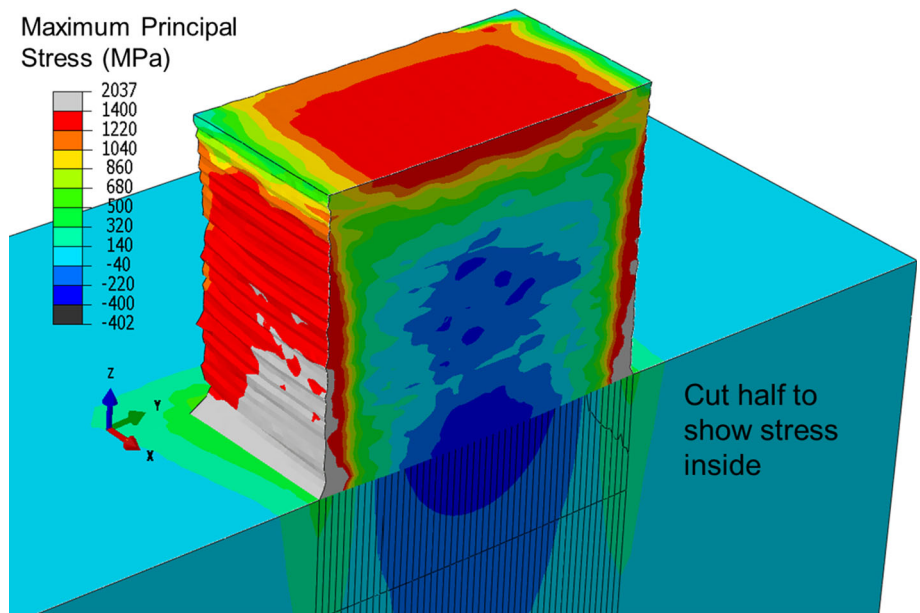


Fig. 17 Predicted temperature distributions during building a bridge sample **a** Heat layers before forming a bridge; **b** Heat a layer near the top surface of the bridge

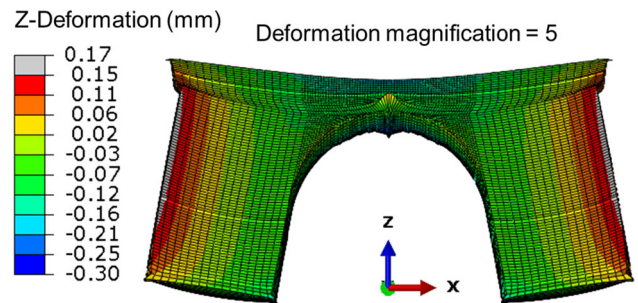


Fig. 18 Predicted final deformation shape for a L-PBF built bridge sample

experimental measured deformations compliment the model prediction.

Layer-heating method took less time than the line-heating method. With the fine mesh, shown in Fig. 13, it took a half day to get one solution. However, the layer-heating method does not require the fine mesh which is needed for moving a heat-source model. Therefore, the layer-heating method can be a potential modeling method to predict residual stress and deformation for L-PBF process for large parts.

6 Conclusions

The objective of this study was to develop modeling methods to predict microstructure, hardness, residual stress, and deformation in large L-PBF built parts by extending modeling methods and theories developed for welding processes. Based on the study, the following conclusions could be drawn:

Fig. 19 Deformation shape of a bridge sample after cutting the sample from the base plate

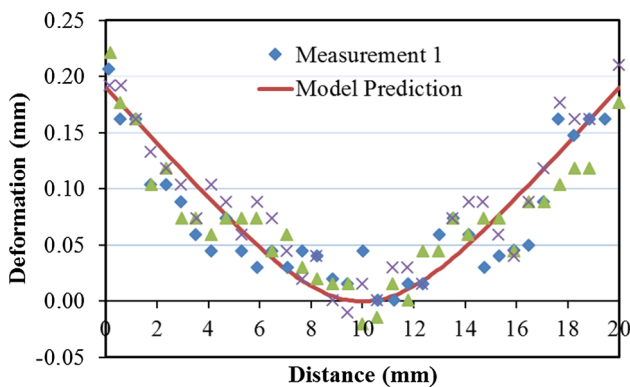
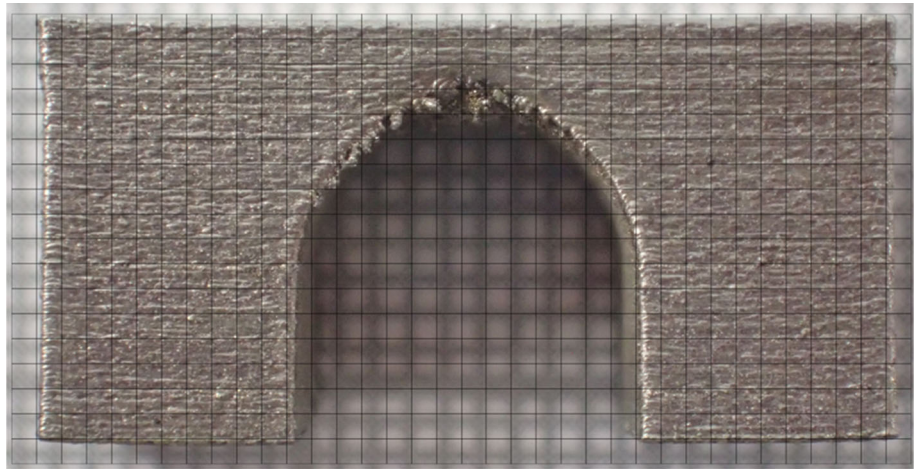


Fig. 20 Deformation magnitudes on the top surface of the bridge sample

- Microstructure and hardness mainly depend on the local geometry in a L-PBF built part. Local models including the interested area could be used to predict microstructure and hardness.
- Microstructure and hardness could be predicted by a sequentially coupled thermal and metallurgical analysis in which moving heat source model is used to accurately predict thermal history.
- Tempering effect must be modeled to accurately predict hardness for an L-PBF built high-strength steel part.
- Residual stress and deformation depends on the structure stiffness. A full model must be used to predict residual stress and deformation for an L-PBF built part.
- Residual stress and deformation could be predicted by a sequentially coupled thermal and mechanical analysis.
- It was found that the line-heating model is unsuitable for analyzing a large L-PBF built part.
- The layer-heating method is a potential method for analyzing a large L-PBF built part.

Acknowledgements This work was funded by the EWI internal research and development program under the Project Tracking Code 56047IRD. Partial experimental data was collected under the EWI Projects 54627IRD and 56590IRD.

References

1. Smith J, Xiong W, Yan W, Lin S, Cheng P, Kafka OL, Wagner GJ, Cao J, Liu WK (2016) Linking process, structure, property, and performance for metal-based additive manufacturing: computational approaches with experimental support. *Comput Mech* 57:583–610
2. Kelly SM, Kampe SL (2004) Microstructural evolution in laser-deposited multilayer Ti-6Al-4V builds: part I. Microstructural characterization. *Metall Mater Trans* 35A:1861–1867
3. Irwin J, Reutzel EW, Michaleris P, Keist J, Nassar AR (2016) Predicting microstructure from thermal history during additive manufacturing for Ti-6Al-4V. *J Manuf Sci Eng* 138(11):111007
4. Vastola G, Zhang G, Pei QX, Zhang YW (2016) Modeling the microstructure evolution during additive manufacturing of Ti6Al4 V: a comparison between electron beam melting and selective laser melting. *JOM* 68(5):1370–1375
5. Smith J, Xiong W, Cao J, Liu WK (2016) Thermodynamically consistent microstructure prediction of additively manufactured materials. *Comput Mech* 57(3):359–370
6. Rodgers TM, Madison JD, Tikare V (2017) Simulation of metal additive manufacturing microstructures using kinetic Monte Carlo. *Comput Mater Sci* 135:78–89
7. Achary R, Sharon JA, Staroselsky A (2017) Prediction of microstructure in laser powder bed fusion process. *Acta Mater* 124:360–371
8. Mukherjee T, Zhang W, DebRoy T (2017) An improved prediction of residual stresses and distortion in additive manufacturing. *Comput Mater Sci* 126:360–372
9. Jamshidinia M, Kong F, Kovacevic R (2013) Numerical modeling of heat distribution in the electron beam melting of Ti-6Al-4V. *J Manuf Sci Eng* 135(6):061010
10. Merceelis P, Kruth JP (2006) Residual stresses in selective laser sintering and selective laser melting. *Rapid Prototyp J* 12(5):254–265
11. Roberts IA, Wang CJ, Esterlein R, Stanford M, Mynors DJ (2009) A three-dimensional finite element analysis of the temperature field during laser melting of metal powders in additive layer manufacturing. *Int J Mach Tools Manuf* 49(12–13):916–923

12. Hodge NE, Ferencz RM, Solberg JM (2014) Implementation of a thermomechanical model for the simulation of selective laser melting. *Comput Mech* 54(1):33–51
13. Nikoukar M, Patil N, Pal D, Stucker B (2013) Methods for enhancing the speed of numerical calculations for the prediction of the mechanical behavior of parts made using additive manufacturing. International solid freeform fabrication symposium, Austin, Texas, USA
14. Patil N, Pal D, Stucker B (2013) A new finite element solver using numerical eigen modes for fast simulation of additive manufacturing processes. International solid freeform fabrication symposium, Austin, Texas, USA
15. Zeng D, Pal D, Patil N, Stucker B (2013) A new dynamic mesh method applied to the simulation of selective laser melting. International solid freeform fabrication symposium, Austin, Texas, USA
16. Seidel C, Zaeh MF, Wunderer M, Weirather J, Krol TA, Ott M (2014) Simulation of the laser beam melting process: approaches for an efficient modelling of the beam-material interaction. *Procedia CIRP* 25:146–153
17. Li C, Fu CH, Guo YB, Fang FZ (2015) Fast prediction and validation of part distortion in selective laser melting. *Procedia Manuf* 1:355–365
18. Papadakis L, Loizou A, Risse J (2014) A computational reduction model for appraising structural effects in selective laser melting manufacturing. *Virtual Phys Prototyp* 9(1):17–25
19. Denlinger ER, Irwin J, Michaleris P (2014) Thermomechanical modeling of additive manufacturing large parts. *J Manuf Sci Eng* 136(6):061007
20. Zeng K, Pal D, Gong HJ, Patil N, Stucker B (2015) Comparison of 3DSIM thermal modeling of selective laser melting using new dynamic meshing method to ANSYS. *Mater Sci Technol* 31(8):945–956
21. Yang YP, Athreya BP (2013) An improved plasticity-based distortion analysis method for large welded structures. *J Mater Eng Perform* 22(5):1233–1241
22. ABAQUS, Version 2017, Dassault Systems, <https://www.3ds.com/products-services/simulia/products/abaqus>
23. Goldak J, Chakravarti A, Bibby M (1984) A new finite element model for welding heat sources. *Metall Trans B* 15(2):299–305
24. Irwin J, Michaleris P (2016) A line heat input model for additive manufacturing. *J Manuf Sci Eng* 138(11):111004
25. Yang YP, Brust FW, Kennedy JC (2002) Lump-pass welding simulation technology development for shipbuilding applications, ASME 2002 pressure vessels and piping conference, Vancouver, BC, Canada. Paper No. PVP2002-1105, pp. 47–54. <https://doi.org/10.1115/PVP2002-1105>
26. Ashby MF, Easterling KE (1982) A first report on diagrams for grain growth in welds. *Acta Metall* 30:1969–1978
27. Ion JC, Easterling KE, Ashby MF (1984) A second report on diagrams of microstructure and hardness for heat-affected zones in welds. *Acta Metall* 32:1949–1962
28. Grange A, Hribal CR, Porter LF (1977) Hardness of tempered martensite in carbon and low-alloy steels. *Metall Trans A* 8(11):1977–1975
29. Yan W, Ge W, Smith J, Lin S, Kafka OL, Lin F, Liu WK (2016) Multi-scale modeling of electron beam melting of functionally graded materials. *Acta Mater* 115:403–412
30. Li C, Fu CH, Guo YB, Fang FZ (2016) A multiscale modeling approach for fast prediction of part distortion in selective laser melting. *J Mater Process Technol* 229:703–712
31. Timken Steel, 4140HW Alloy Steel Technical Data. http://www.timkensteel.com/~media/4140HW_Brochure_July2015_Update
32. JMatPro, Version 6.2, Sente Software Ltd, <http://www.sentesoftware.co.uk/jmatpro.aspx>
33. Special Metal, Inconel alloy 718. http://www.specialmetals.com/assets/smc/documents/inconel_alloy_718.pdf